Enhanced localization and protection of topological edge states due to geometric frustration

L. Madail,[1] S. Flannigan,[2] A. M. Marques,[1] A. J. Daley,[2] and R. G. Dias[1]

[1]*Department of Physics & I3N, University of Aveiro, 3810-193 Aveiro, Portugal.*
[2]*Department of Physics & SUPA, University of Strathclyde, Glasgow G4 0NG, United Kingdom.*

(Dated: June 27, 2019)

Topologically non-trivial phases are linked to the appearance of localized modes in the boundaries of an open insulator. On the other hand, the existence of geometric frustration gives rise to degenerate localized bulk states. The interplay of these two phenomena may, in principle, result in an enhanced protection/localization of edge states. In this paper, we study a two-dimensional Lieb-based topological insulator with staggered hopping parameters and diagonal open boundary conditions. This system belongs to the C_{2v} class and sustains 1D boundary modes except at the topological transition point, where the C_{4v} symmetry allows for the existence of localized (0D) corner states. Our analysis reveals that, while a large set of boundary states have a common well defined topological phase transition, other edge states reflect a topological non-trivial phase for any finite value of the hopping parameters, are completely localized (compact) due to destructive interference and evolve into corner states when reaching the higher symmetry point. We consider the robustness of these compact edge states with respect to time-dependent perturbations and indicate ways that these states could be prepared and measured in experiments with ultracold atoms.

PACS numbers: 74.25.Dw

I. INTRODUCTION

Recently, the charge polarization theory based on topological invariants has been extended to include new symmetry protected topological phases in crystalline insulators of dimension dD characterized by the existence of quantized n-order moments that reflect the presence of surface modes of dimension $(d-n)D$ [1–3]. For example, in 2D systems with open boundary conditions (OBC) such that C_{4v} symmetry is present, quantized quadrupole moments underly the presence of corner states in the band gaps [1–3]. If OBC lead to lower symmetries (C_{2v} for instance), one expects to observe typical weak topological insulator behavior with vertical and horizontally localized boundary modes. Ultimately, geometric frustration in 2D lattices may enrich this topological description by allowing an enhancement of the edge states localization [4, 5].

In this paper, we study a Lieb-type system with staggered hopping terms (t_1 and t_2). This model exhibits a non-centered rotation axis within the unit cell which is responsible for non-quantized topological indexes [6]. When the choice of OBC generates a lattice with C_4 symmetry, the non-trivial topological regime reveals corner localized states. Our work focuses on a different type of boundary under which the model has C_2 rotational symmetry in the lattice when $t_1 \neq t_2$ and a singular C_4 rotational symmetry for identical hopping parameters. In this model, a particular boundary mode arises displaying complete localization due to wavefunction destructive interference, similar to compact localized flat band bulk states [7]. Since this state has support in more than one sublattice it will acquire non-zero energy without the introduction of local potentials. This automatically implies that the symmetry that protects these states is not usual chiral symmetry associated with bipartite lattices. In fact, one can show that this state is related to the square-root topological insulator [8–13] and the protecting symmetry is a sublattice chiral-like hidden symmetry. To our knowledge, topological characterization of a weak topological insulator with compact edge states has not been addressed in the literature where geometrically frustrated lattices are studied [14–16]. In our paper, we show that these compact localized states reflect a different topological transition point (the atomic limit in our case) and consequently they remain completely localized (in the system boundaries, edge or corner) even at the usual transition point $t_1 = t_2$ where the remaining edge states converge. Our topological characterization follows the approach of [6] which agrees with other methods to address topological invariants that protect finite energy edge states in the case of non-commensurate OBC or non-centered I-axis in the unit cell such as the modified approaches of splitting the Zak's phase into intracell and intercell contributions [17–21], the squaring of the Hamiltonian [8–13] and synthetic dimensions [22–26]. The robustness of this compact state is probed when applying a time dependent perturbation to the hopping amplitudes in order to examine its protection against mixing with the bulk states and test the viability of its preparation in a cold atom experiment.

II. STAGGERED HOPPING TERMS IN THE LIEB LATTICE

The Lieb lattice is a decorated line-centered square lattice characterized by three species of atoms (A,B,C) per unit cell where electrons can hop between nearest-neighbor atoms [27, 28]. This system will have two types of states according to the degree of localization of the wavefunction in the system: bulk states which span through all possible k-values and plaquette localized states of zero energy. In order to observe topological phase transitions with the emergence of edge states, staggered hopping terms are required and therefore we have to consider a larger unit cell of 6 sites (in the original

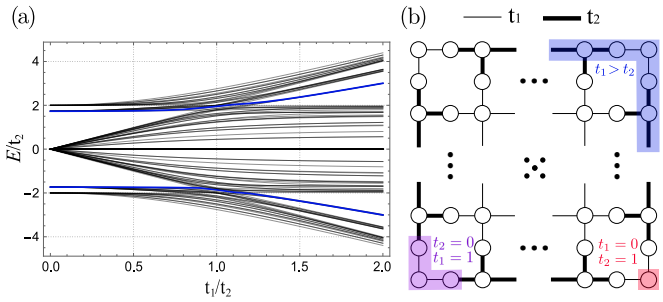

Figure 1. (a) Plot of the energy spectrum for the Lieb lattice with conventional OBC and integer number of plaquettes as a function of the ratio t_1/t_2. (b) Schematic illustration of corner states present in the Lieb lattice according to the choice of hopping amplitudes: $t_1 = 0$ (red); $t_2 = 0$ (purple) and $t_1 > t_2$ (blue).

lattice these will correspond to two A, B and C sites). Using OBC such that we have a system with integer number of plaquettes will result in the creation of two distinct topological regimes. In one of these, when $t_1 > t_2$, 4 isolated degenerate states appear in the bandgap and are localized in the corners of the lattice [see blue curves of Fig. 1(a)]. These degenerate states reflect all the possible combinations of parity values in both x and y directions. Note that, C_4 symmetry is preserved in the lattice independently of the values $\{t_1, t_2\}$. The localization of this state in the corner depends on the ratio $t = t_1/t_2$ and will be less extended in the lattice the greater the value of t. Specifically, in the limit $t_1 = 0$ the corner site can host a zero-energy localized state. On the other hand, if $t_2 = 0$ we get a three-site cluster in the corner with energies $\varepsilon = \{0, \pm\sqrt{2}t_1\}$ [see Fig. 1(b)].

We now consider OBC that diagonally cross the Lieb plaquettes [see Fig. 2(b,c)], resulting in the unit cell of Fig. 2(a). In this case, corner sites share both t_1 and t_2 hopping terms. This means that, whenever one of the hopping terms vanishes we will have three-site clusters in the vertical/horizontal boundaries hosting finite energy compact edge states and the corner states will only be seen when the Hamiltonian has C_4-rotation symmetry ($t_1 = t_2$).

The tight-binding Hamiltonian for this system is given by

$$H_{TB} = \sum_{m,n} t_1 a^\dagger_{m,n}(b_{m,n} + c_{m,n} + d_{m-1,n} + e_{m-1,n}) + t_2 f^\dagger_{m,n}(b_{m,n} + d_{m,n} + c_{m,n+1} + e_{m,n+1}) + h.c., \quad (1)$$

where $\alpha^\dagger_{m,n}$ is the fermionic creation operator acting at site $\alpha = (a,b,c,d,e,f)$ of unit cell index (m,n). In order to obtain the dispersion relation of the Lieb lattice assuming periodic boundary conditions we proceed by performing the Fourier transform on the operators of Eq.1 using

$$\boldsymbol{\alpha}_{k_x,k_y} = \frac{1}{\sqrt{MN}} \sum_{m,n} \boldsymbol{\alpha}_{m,n} e^{i(k_x m + k_y n)} \quad (2)$$

where $\boldsymbol{\alpha}_\xi = \left(a_\xi, b_\xi, c_\xi, d_\xi, e_\xi, f_\xi\right)^T$, ξ labels the 2D coordinates $\{m,n\}$ or the momentum space $\{k_x, k_y\}$, M and N are the number of unit cells in the (x,y)-directions, respectively.

The k-space Hamiltonian can be found by transforming the tight-binding Hamiltonian by

$$H_{TB} = \sum_{k_x,k_y} (\boldsymbol{\alpha}^\dagger_{k_x,k_y})^T H_{\mathbf{k}} \boldsymbol{\alpha}_{k_x,k_y}, \quad (3)$$

with

$$H_{\mathbf{k}} = \begin{pmatrix} 0 & t_1 & t_1 & t_1 e^{-ik_x} & t_1 e^{-ik_x} & 0 \\ t_1 & 0 & 0 & 0 & 0 & t_2 \\ t_1 & 0 & 0 & 0 & 0 & t_2 e^{-ik_y} \\ t_1 e^{ik_x} & 0 & 0 & 0 & 0 & t_2 \\ t_1 e^{ik_x} & 0 & 0 & 0 & 0 & t_2 e^{-ik_y} \\ 0 & t_2 & t_2 e^{ik_y} & t_2 & t_2 e^{ik_y} & 0 \end{pmatrix} \quad (4)$$

where $k_x(k_y) = 2\pi p/M(N)$ for $p = 1, \ldots, M(N)$. The spectrum of $H_{\mathbf{k}}$ is the set of eigenvalues of this 6×6 matrix, giving the general expression for the dispersion relation with the following six distinct bands

$$E_\pm(k_x,k_y) = \pm\sqrt{2}\sqrt{(1+t^2) \pm \sqrt{t^4 + 1 + t^2(-1 + \Lambda_{k_x,k_y})}},$$
$$E_0(k_x,k_y) = 0. \quad (5)$$

with $\Lambda_{k_x,k_y} = \cos k_y + \cos k_x(1 + \cos k_y)$ and $t = t_2/t_1$ [note that $E_0(k_x,k_y)$ is $2\times$-degenerate]. The band structure for this system is similar to that of the usual Lieb system for equal hopping parameters [Fig.3(a)], displaying electron-hole symmetry and a Dirac cone at the high symmetry point $\Gamma = (\pi,\pi)$. When $t_2 \neq t_1$ [Fig.3(b)], two band gaps are created in the top and bottom bands where boundary modes may emerge.

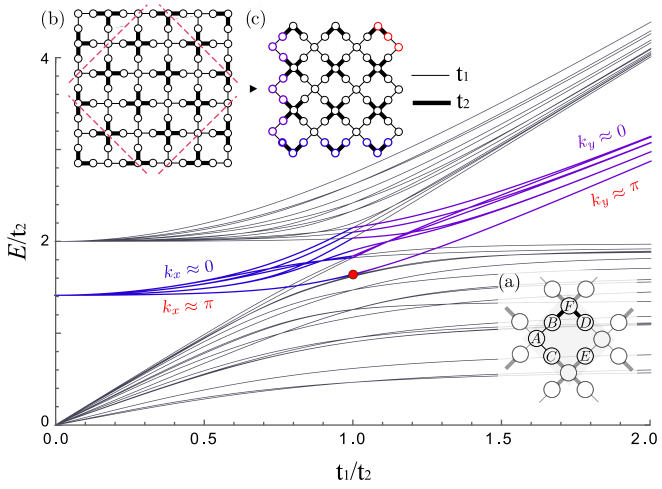

Figure 2. Boundary states of the Lieb rotated lattice. In the top-left, we schematize the creation of the rotated lattice with unit cell of (a) from the two-dimensional Lieb model (b) where the boundaries belong to a $\pi/4$ rotated $x-y$ reference frame (c). The energy spectrum as a function of the hopping parameters is plotted for the rotated Lieb lattice with 5×5 plaquettes and $t_2 = 1$ (only the positive energy range is shown). We identify the different types of states according to their localization in the lattice: bulk (black line), vertical (purple line), horizontal (blue line) and corner (red dot) states. This last state appears only for $t_1 = t_2$, when C_4 rotation symmetry is restored.

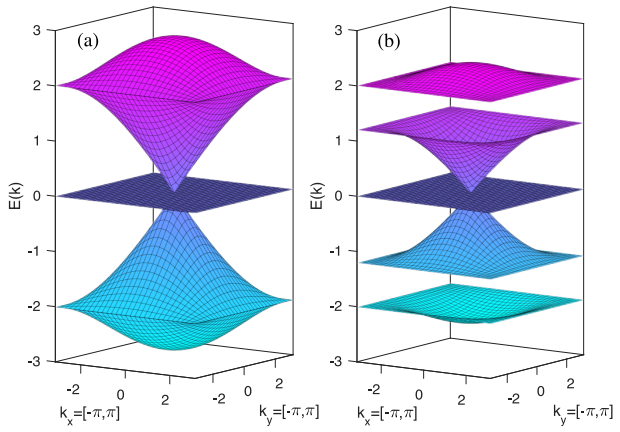

Figure 3. Dispersion relation of the Lieb rotated lattice for $t_2 = 1$ and (a) $t_1 = t_2$; (b) $t_1 = 1.67t_2$.

Considering the system with OBC shown in Fig. 2(c), the resulting Lieb cluster with integer number of plaquettes holds C_2 rotational symmetry for any choice of the hopping terms except when $t_1 = t_2$, where C_{4v} symmetry is restored. As a result, this system behaves as a weak topological insulator [29] since it carries horizontal or vertically localized states whenever $t_1 \neq t_2$. In fact, due to the absence of magnetic flux, the time-reversal symmetry is preserved and the Chern number is zero [30]. The band of edge states disappears at the gap closing point except for one particular state which does not participate in the level crossing at the topological transition point. The latter leads to the appearance of the corner state when $t_1 = t_2$ marking the evolution of maximally localized horizontal to vertical edge modes (see Fig. 2).

III. LOWER DIMENSIONAL SYSTEMS

In this section we will address lower-dimensional systems based on the Lieb unit cell. Since they maintain $\{M_x, M_y\}$ reflection symmetries, they will be similar to the square rotated Lieb lattice from the symmetry point of view and thus studying its topology will allow us to comprehend the different types of edge states previously identified. Through this analysis we make use of the vertical mapping – a basis rotation which combines Wannier states of sites that intersect the same vertical axis. We define the orthonormal basis space $B_{I_\gamma} = \{|\psi_{I_1}\rangle, \ldots, |\psi_{I_{N_\gamma}}\rangle\}$ for each set $\mathscr{S}_\gamma$ of all I_m sites in the γ-vertical axis with $\dim \mathscr{S}_\gamma = N_\gamma$, with the following conditions

$$\begin{cases} |\psi_{I_i}\rangle = \dfrac{1}{\sqrt{\beta}} \displaystyle\sum_{m=1}^{N_\gamma} a_m |\psi_{I_m}\rangle, \\ \langle \psi_{I_i} | \psi_{I_j}\rangle = 0, \qquad i \neq j. \end{cases} \tag{6}$$

Specifically when N_γ is even, we get $\beta = N_\gamma$ and $a_m^* a_m = 1$ for all $m = 1, \ldots, N_\gamma$. As an example, a vertical axis with $N_\gamma = 4$ sites requires a set with $\dim \mathscr{S}_\gamma = 4$ vectors, each with unitary amplitude components $a_m = \pm 1$ such that all 4 vectors of the basis for that γ-axis are orthogonal. For an odd number of vertical sites in the set $\mathscr{S}_\gamma$, the components are chosen to be the smallest integer amplitudes possible, respecting the vertical reflection symmetry and the orthogonality rule.

The topological characterization follows the generalization of the Zak's phase in [6] for systems with a non-centered symmetry point. For the determination of this topological invariant we rely on the inversion symmetry present in the system. In such case, the well-quantized Zak's phase is given by the parity of the occupied Bloch wave functions at the inversion invariant points in the Brillouin zone [31] plus a correction accounting for the displacement of the inversion center with respect to the midpoint of the unit cell.

A. Lieb rhombi chain

The Lieb rhombi chain is a quasi-1D system consisting of Lieb rotated plaquettes connected at the vertices with 7 sites per unit cell [see Fig. 4(a)]. The bulk Hamiltonian is followed by

$$H_k = \begin{bmatrix} 0 & t_1 & t_1 & e^{-ik}t_1 & e^{-ik}t_1 & 0 & 0 \\ t_1 & 0 & 0 & 0 & 0 & t_2 & 0 \\ t_1 & 0 & 0 & 0 & 0 & 0 & t_2 \\ e^{ik}t_1 & 0 & 0 & 0 & 0 & t_2 & 0 \\ e^{ik}t_1 & 0 & 0 & 0 & 0 & 0 & t_2 \\ 0 & t_2 & 0 & t_2 & 0 & 0 & 0 \\ 0 & 0 & t_2 & 0 & t_2 & 0 & 0 \end{bmatrix}, \tag{7}$$

where we write the energy dispersion relation as

$$\begin{aligned} E_\pm(k) &= \pm\sqrt{\left(2t_1^2 + t_2^2\right) \pm \sqrt{4t_1^2 t_2^2 \cos(k) + 4t_1^4 + t_2^4}}, \\ E_{t_2}(k) &= \pm\sqrt{2}t_2, \\ E_0(k) &= 0. \end{aligned} \tag{8}$$

When $t_1 = t_2$, the band structure shows three flat bands $\varepsilon_k = \{0, \pm\sqrt{2}\}$ and four dispersive bands touching at $k = \{0, \pi\}$ [see Fig. 4(c)]. For the particular case of $k = 0$ [see Fig. 4(e)], this gap closing point is robust against perturbations that preserve the inversion symmetry. The same is not seen in Fig. 4(d) for $k = \pi$. In this case, gaps open at $t_1 \geq t_2/\sqrt{2}$ and edge states may appear depending on the choice of boundary conditions.

Making use of the vertical combination mapping [see Fig. 4(b)] of Eq.6 (which, in this case, corresponds to a bonding and anti-bonding combination since $N_\gamma \leq 2$) [32], the system can be rewritten as a $\sqrt{2}t_1 t_2 t_2 \sqrt{2}t_1$ chain and a chain of decoupled three-site clusters with a single hopping parameter dependence t_2, responsible for the flat bands E_{t_2} of Eq.8. Since the topological transition of the $t_1 t_2 t_2 t_1$ chain occurs at $t_1 = t_2$ [6], our top mapped chain of Fig. 4(b) holds a topological transition point at $t_1 = t_2/\sqrt{2}$. The chain of decoupled clusters may as well be interpreted as a $t_1 t_2 t_2 t_1$ chain, adding

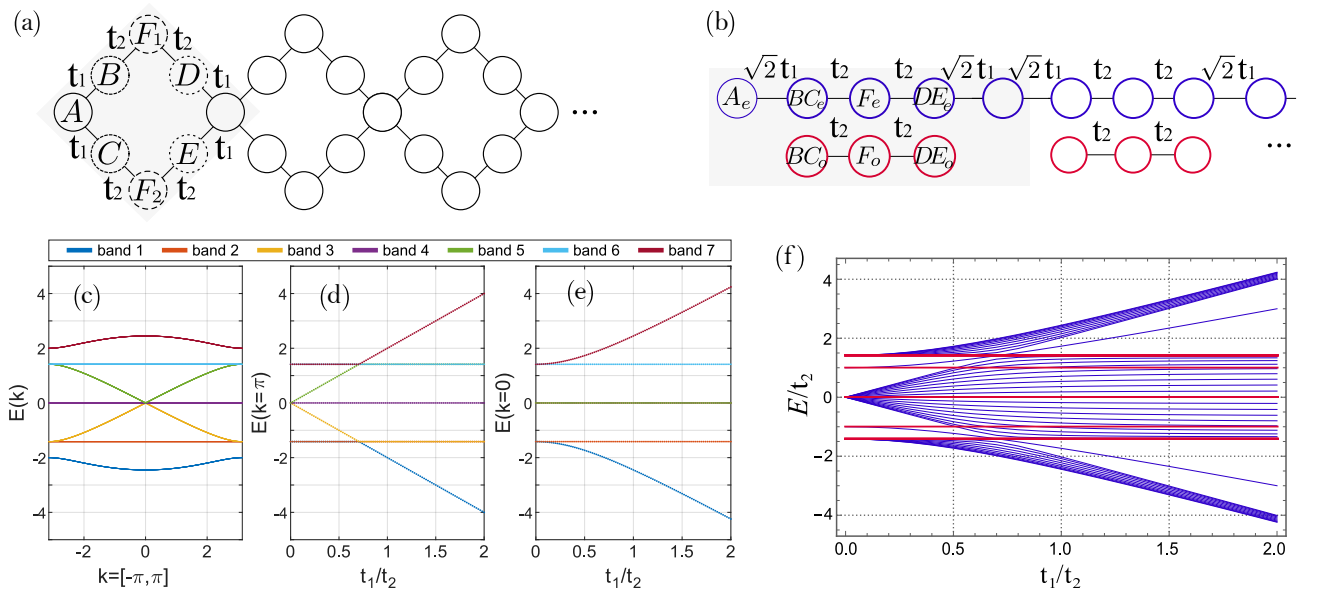

Figure 4. Lieb rhombi chain with 7 sites per unit cell. (a) original model; (b) mapped version of the vertical bonding (blue) and anti-bonding (red) combination basis with a continuous chain of even states (e) and decoupled chains of odd states (o). (c,d,e) plot the dependence of the band structure with the hopping parameters. In (c) we plot the band structure for $t_1 = t_2 = 1$ and in (d) and (e) we show the dependence with t_1/t_2 of the $k = \pi$ and $k = 0$ levels, respectively. The plot in (f) represents the eigenstates of each (blue and red) chains as a function of the hopping parameters for an open chain (a) with left-A and right-F endings. The edge states in the band gaps evolve from the topological transition $t_1 = \sqrt{2}t_2$ (blue line) and from the atomic limit (red line).

fictional A_o sites connected to the clusters by a $t_1 = 0$ hopping term, implying a topological transition at the atomic limit $t_2 = 0$.

One may choose appropriate OBC such that both independent systems host edge states localized at least in one of their boundaries [see Fig. 4(f)]. In such case, the top chain requires left and/or right A_e ending sites in the regime $\sqrt{2}t_1 > t_2$ and left and/or right F_e ending sites for $\sqrt{2}t_1 < t_2$ in order for the localized edge states to be observed. On the other hand, the decoupled three-site cluster chain will display edge states with energy $\varepsilon = \pm t_2$ when OBC are such that a two-site cluster is generated at least in one end of the chain (i.e. the chain should end with a left and/or right F_o site). Moreover, when a single site cluster is constructed, we will also have an edge state with zero energy, albeit not protected against perturbations since it overlaps with zero-energy flat bands present in the system.

Although our model is a quasi-1D chain, the Zak's phase can still be calculated if one follows the method of [6] for 1D-chains with non-centered inversion point with additional considerations. Fig. 5 specifies the inversion center $r_c = a(1/2 + m/2N_x)$ with $N_x = 4$ being the number of sites encountered in the x-direction of the $\sqrt{2}t_1t_2t_2\sqrt{2}t_1$ mapped chain and m the displacement of the inversion axis with respect to the center of the unit cell. We may choose one of the two axis (r_{c_1} or r_{c_2}) with respective $m = 1$ and $m = -3$ (the Zak's phases for the two inversion axis suffer a shift of $\tilde{\mathscr{Z}}_{j,r_{c_2}} - \tilde{\mathscr{Z}}_{j,r_{c_1}} = \pi$). The corrected Zak's phase for the Lieb rhombi chain reads

$$\mathscr{Z}_j = \begin{cases} \arg\left(p_0 p_\pi^\dagger\right) + \sum_{N-m'+1}^{N} \int_0^\pi dk |u_j(k,|m'|)|^2, & m < 0, \\ \arg\left(p_0 p_\pi^\dagger\right) - \sum_{1}^{m'} \int_0^\pi dk |u_j(k,|m'|)|^2, & m > 0, \end{cases} \tag{9}$$

for each band j where m' is the evaluated number of k-dependent terms in the inversion operator for each displacement m (see [6]) and $N = 7$ the number of sites in the unit cell of the Lieb chain. We gather the results for the Zak's phase of each band in Table I for r_{c_1} taking into account the two topological regimes previously mentioned. From one regime to the other, we see a π-shift of the Zak's phase of the dispersive bands and this is consistent with the results achieved for a $t_1t_1t_2t_2$ chain in [6]. Furthermore, since there is no gap opening or closing for $k = 0$, the parity values p_0 for each band remain constant for the two topological regimes. For the flat bands arising from the three dangling sites in the unit cell, the two different regimes will not introduce a π-shift because the respective flat bands remain gapped. This reflects the fact that the topological transition for this chain of clusters occurs when $t_2 = 0$. If we choose a different unit cell which does not contain three connected dangling sites the Zak's phase is shifted by π.

It can be shown that, through an appropriate rotation of the BC_o and DC_o sites, the chain of decoupled three-site clusters at the bottom of Fig. 4(b) becomes a diamond chain with a single renormalized hopping parameter, $t_2/\sqrt{2}$, and a π-flux per plaquette [33]. Recently, this model was found

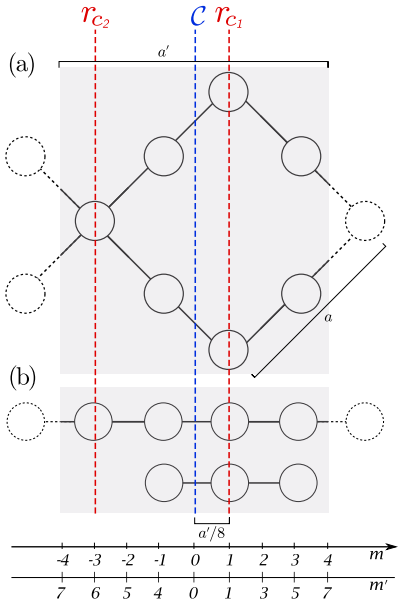

Figure 5. Determination of index m' for the calculation of the Zak's phase. We specify the unit cell center (blue line) as well as the two possible inversion center axis (red line) for both the original (a) and mapped (b) rhombi chain.

		r_{c_1}		
	band	$\tilde{\mathscr{Z}}_j$	p_0	p_π
$t_1 < t_2/\sqrt{2}$	1	0	1	1
	2	0	1	1
	3	π	1	-1
	4	0	-1	-1
	5	0	-1	-1
	6	0	1	1
	7	0	1	1
$t_1 > t_2/\sqrt{2}$	1	π	1	-1
	2	0	1	1
	3	0	1	1
	4	0	-1	-1
	5	π	-1	1
	6	0	1	1
	7	π	1	-1

Table I. Calculation of the corrected Zak's phase ($\tilde{\mathscr{Z}}_j$) and parity values $\{p_0, p_\pi\}$ for each band j of Fig. 4(c) and for the two topological regimes using the inversion center r_{c1}.

to fall into a new category of topological insulators labeled Square-Root Topological Insulators ($\sqrt{TI}$s) [8, 9]. The non-trivial topological features of these $\sqrt{TI}$s are linked to their squared-Hamiltonian (H^2) [34, 35]. Since $\sqrt{TI}$s are bipartite, their H^2 can be put into a block diagonal form, that is, the squared model is a system of two-independent chains, one of which being topologically non-trivial. Under the square-root operation, the topological states of the squared model are then mapped into the corresponding states of the original $\sqrt{TI}$ model. Through the basis rotation mentioned above, our three-site cluster model directly inherits the same topological nature as that of the diamond chain with π-flux per plaquette.

B. Lieb rhombi ribbon with single-direction PBC

In the Lieb rhombi chain, we showed the existence of two topological transitions, one of which occurs at the atomic limit and leads to a state exclusively in the topological non-trivial regime. We will now study a more complex system - the Lieb rhombi ribbon composed by several rhombi chains connected at the F-sites (see Fig. 6) - and show that similar behavior is also present.

Let us first consider a horizontal cylinder where PBC are applied in the y-direction and OBC in the x-direction preserving an integer number of plaquettes [see Fig. 6(a)]. The y-momentum is a good quantum number and one can interpret this system as a set of 1D chains indexed by k_y. Using the unit cell indexation of Fig. 2(a), we write the Hamiltonian of each m-chain as

$$H_{TB}(m,k_y) = \sum_{m,k_y} t_1 a^\dagger_{m,k_y}(b_{m,k_y} + c_{m,k_y} + d_{m-1,k_y} + e_{m-1,k_y}) +$$
$$t_2 f^\dagger_{m,k_y}(b_{m,k_y} + d_{m,k_y} + e^{-ik_y} c_{m,k_y} + e^{-ik_y} e_{m,k_y}) + h.c. \quad (10)$$

The effective unit cell of each of these 1D chains is now composed by two diamond plaquettes connected at F-sites [see Fig. 7(i)]. Similarly to the system addressed by Kremer *et al.* [9], we encounter a Peierls phase factor [36] in one of the hopping terms of each diamond plaquette which translates into a magnetic flux inside each loop. In this case, however, consecutive plaquettes have opposite flux directions. Using bonding and anti-bonding combinations of B (D) and C (E) states, we arrive at a bonding $\tilde{t}_1\tilde{t}_2\tilde{t}_2\tilde{t}_1$ chain [$\tilde{t}_1 = \sqrt{2}t_1$ and $\tilde{t}_2 = \sqrt{2}t_2\cos(k_y/2)$] with additional anti-bonding sites connected to the F-sites by an effective $\tilde{t}_3 = \sqrt{2}t_2\sin(k_y/2)$ [see Fig. 7(ii)]. In the particular case of $k_y = 0$, the system falls into the topological behavior of a $t_1t_2t_1$ chain [see Fig. 7(ii$_1$)]. For $k_y = \pi$ the effective hopping $\tilde{t}_2 = 0$ leads to two chains of decoupled three-site clusters with $\tilde{t}_1$ and $\tilde{t}_3$ hopping terms, respectively [see Fig. 7(ii$_2$)]. We encounter the same description as in the Lieb rhombi chain, where the topological transition point occurs at the atomic limit. Therefore, three flat bands are created for each hopping parameter and edge states emerge every time OBC are such that break these clusters into two-site boundaries. As expected, an edge band of all possible k_y-values appears in the band gap for $t = t_1/t_2 > 1$, when the system ends at A-sites. These edge states have the same energy at the transition point $t = 1$, except for the $k_y = \pi$ edge state that will instead cross the bulk band at $t = \sqrt{2}$. This behavior is observed in Fig. 6 where we plot the energy spectrum of the ribbon considering PBC in the y-direction and a unit cell

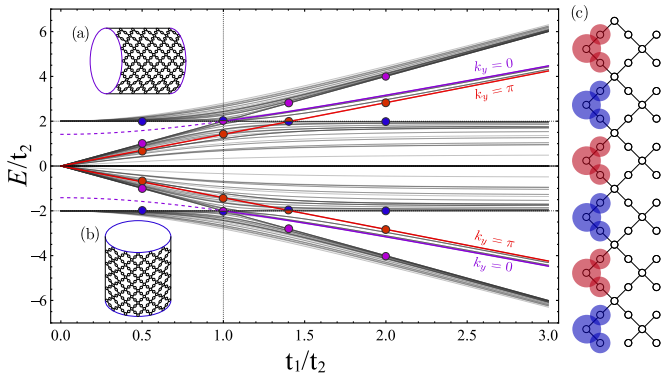

Figure 6. Plot of the energy spectrum for the rotated Lieb ribbon with OBC in the x-direction and PBC in the y-direction as a function of the ratio t_1/t_2. (a) and (b) schematically illustrate the PBC in the y and x direction, respectively (the colors in the boundaries of the cylinders represent the type of edge states energies of Fig. 2 supported by each system). The plot was computed for system in (a) with 5 plaquettes in the x-direction where we overlap the analytical form of the edge states for $k_y = 0$ (purple line) and $k_y = \pi$ (red line). Due to the chosen terminations for the numerical evaluation, we will not see the $k_y = 0$ edge state level in regime $t_1 < t_2$ (dashed line). The colored dots correspond to those of Fig. 7. In (c) we represent the particular case of $k_y = \pi$ state with total localization in the left boundary and no bulk decay.

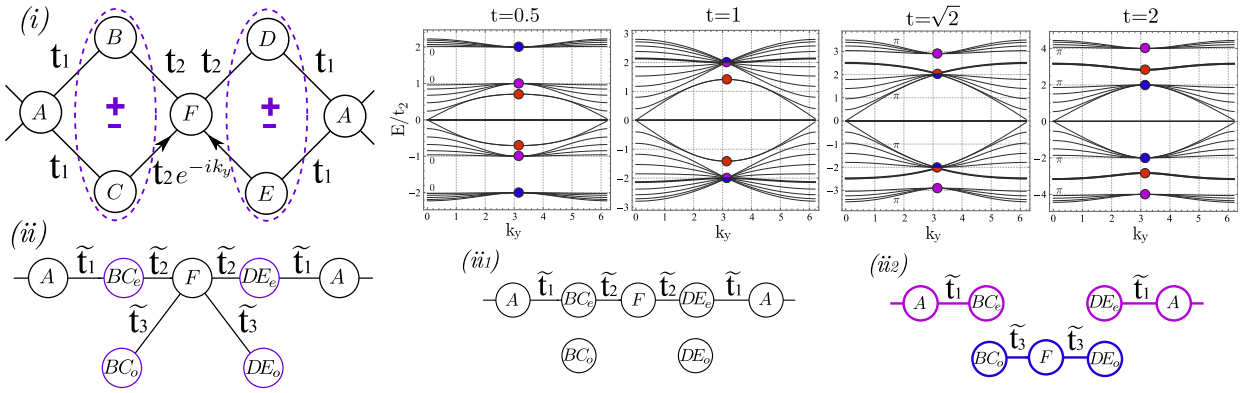

Figure 7. Effective 1D-chains categorized by k_y-values. The Lieb rhombi ribbon after Fourier transforming in the periodic y-direction maps into a diamond chain *(i)* with opposite magnetic flux in consecutive plaquettes, yielding k_y-dependent hopping terms between F and both C and E sites. A basis rotation via bonding and anti-bonding linear combination of B (D) and C (E) states gives chain *(ii)* with effective hopping terms $\tilde{t}_2(k_y)$ and $\tilde{t}_3(k_y)$. At the inversion-invariant momenta $k_y = \{0,\pi\}$ we arrive at a $\sqrt{2}t_1\sqrt{2}t_2\sqrt{2}t_2\sqrt{2}t_1$ chain *(ii$_1$)* and a set of $\sqrt{2}t_1\sqrt{2}t_1$ and $\sqrt{2}t_2\sqrt{2}t_2$ clusters *(ii$_2$)*, respectively. The right figures plot the energy spectra as a function of k_y (and respective corrected Zak's band phase [6]) for a system (i) with 10 diamond plaquettes, spanning different $t = t_1/t_2$ values. We identify the band of edge states (thick black line) which becomes present in the non-trivial topological regime, the $k_y = \pi$ flat band states (purple and blue dots) for each cluster of *(ii$_2$)* and the $k_y = \pi$ edge state (red dot), which will not converge to the band gap closing point at the topological transition $t = 1$.

with 5 plaquettes in the y-direction. The appearance of energy levels in the middle of the band gap is only seen for the case where t_1 outgrows t_2. These edge states are confined to the open vertical boundaries of the ribbon and we show below that they are approximately the vertical edge states observed for the square Lieb cluster of Fig. 2.

In the case of a 2D Lieb system, the general form of edge-like states should include two independent decaying behaviors $\{c_x, c_y\}$ such that the components of the edge state in a unit cell are given by $|u_{l,j}\rangle = c_x^l c_y^j(\psi_A, \psi_B, \psi_C, \psi_D, \psi_E, \psi_F)^T$ with indexes (l, j) denoting the unit cell of 6 sites [see Fig. 2(a)]. Imposing PBC in the y-direction implies $c_y = e^{ik_y}$ and $k_y = \{0,\pi\}$ will define the top and bottom levels of the edge states band (see Fig. 6).

The OBC of the horizontal Lieb cylinder of Fig. 6(a) imply $\{B,C\}$ and $\{D,E\}$ virtual sites of zero amplitude [37] at the left and right ends, respectively. The solutions for the decaying behaviors are obtained by solving the eigenvalue relations and setting the amplitudes in these sublattices to zero. For $k_y = \{0,\pi\}$, the set of solutions is shown in Table II with $\beta_0^t = \sqrt{2}\sqrt{t^2+1}$, $\beta_1^t = \sqrt{2}/(t\sqrt{1+t^2})$ and $\beta_2^t = \sqrt{t^2+1}/\sqrt{2}$.

k_y	c_y	c_x	ε	$\lvert\varepsilon\rangle$
0	1	$-t^2$	$-\beta_0^t$	$(\beta_1^t,0,0,-\beta_1^t,1,1)^T$
			β_0^t	$(-\beta_1^t,0,0,\beta_1^t,1,1)^T$
		$-1/t^2$	$-\beta_0^t$	$(t,-\beta_2^t,-\beta_2^t,1,0,0)^T$
			β_0^t	$(t,\beta_2^t,\beta_2^t,1,0,0)^T$
π	-1	0	$-\sqrt{2}t$	$(-\sqrt{2},1,1,0,0,0)^T$
			$\sqrt{2}t$	$(\sqrt{2},1,1,0,0,0)^T$

Table II: Edge-like behavior of $|u_{l,j}\rangle$ assuming PBC in the y-direction and decaying behavior from either ends of the open x-direction ($c_x < (>) 1$ for left (right) edge localization). These states are only present when the virtual sites at the respective edge coincide with the zeros of amplitude of $|u_{l,j}\rangle$.

Note we have neglected solutions with energies that fall into the bulk bands. A $k_y = 0$ ($c_y = 1$) state will have two possible decaying behaviors in the x-direction $c_x = \{-t^2, -1/t^2\}$ depending on the hopping constants. In the $t > 1$ regime, a $c_x = -t^2$ ($c_x = -1/t^2$) decaying factor will give a right (left) edge state in which the degree of localization will increase with t ($1/t$).

For a non-zero c_x, the eigenfunctions will always have dependence with both t_1 and t_2 and hence the respective topological transition occurs at a finite value of $t = t_1/t_2$ where the edge states become extended. The same will not be seen for $k_y = \pi$ ($c_y = -1$) where the only possible edge-like states have decay $c_x = 0$ (it is implicit that $l = 0, 1, \cdots N-1$), which implies that the state is completely localized in the first column of Lieb plaquettes [see Fig. 6(c)]. All these conclusions are intuitively found in the plot of Fig. 6, where we show the exact overlap of the eigenvalue solutions for $k_y = \{0,\pi\}$ edge states (purple and red curves, respectively) onto the numerical calculations of the Lieb rhombi ribbon with 5×5 plaquettes and PBC in the y-direction.

This procedure can be replicated for the system of Fig. 6(b), where PBC are applied in the x-direction. Indeed, since the open boundaries in this case end with t_2 hopping terms, both the top and bottom edge states appear when $t_1 < t_2$. Thus, the analytical results can be inferred by simply taking the transformation $t_1 \leftrightarrow t_2$, yielding $c_y \in \{(-t^2, -1/t^2), 0\}$ for $k_x \in \{0,\pi\}$.

IV. ROTATED LIEB SQUARE LATTICE

So far, we have studied the rotated Lieb square lattice with the application of PBC to one of the boundaries of the system and found the edge-like states in the open direction. Since the square lattice has t_1 (t_2) terminations in the y-(x-)direction

(see Fig. 2), the above analysis allows us to predict the behavior of the square lattice for both $t_1 < t_2$ and $t_1 > t_2$ regimes. In Fig. 2, the top and bottom levels of the edge states band correspond to $k_{x/y} \approx \{0, \pi\}$ states that have similar behavior to those obtained for the Lieb ribbon. When $t_1 > t_2$ ($t_1 < t_2$), they are localized in the vertical (horizontal) boundaries. In the specific case of $k \approx 0$, when $t_1 > t_2$, these vertical boundary modes have a bulk oriented decay $c_x = -t^2$ for a right localized state and $c_x = -1/t^2$ for a left localized state. Analogously, for $t_1 < t_2$, we find horizontal edge states with decay $c_y = -t^2$ ($c_y = -1/t^2$) for a top (bottom) localization.

The $k_{x/y} \approx \pi$ states of Fig. 2 drift away from the remaining levels of the edge states band as t_1/t_2 approaches the topological transition ($t_1/t_2 = 1$), since the latter levels converge to the band closing point (this is more clearly observed for larger cluster sizes). From the previous results, we identify this state to have a decaying behavior $c = 0$ for both topological regimes, meaning it is entirely localized in a single boundary (or unit cell if PBC are considered in the perpendicular direction of maximum localization). For the limiting cases $t_1 \gg t_2$ and $t_1 \ll t_2$, the energy eigenvalues found using periodic conditions $\varepsilon_a = \pm\sqrt{2}t_1$ and $\varepsilon_b = \pm\sqrt{2}t_2$ are good approximations for this boundary mode in the square lattice. Nevertheless, around point $t_1 = t_2$, the energy curve will, in principle, be ruled by a function $f(\varepsilon_a, \varepsilon_b)$. At this point, corner states are generated due to the increase in symmetry (the square lattice holds a 4-fold rotational symmetry when both hopping terms are equal) and reflect the evolution of maximum localized horizontal $k_x \approx \pi$ to vertical $k_y \approx \pi$ edge states which do not fall into a topological transition point. In all, these corner states are a manifestation of the emergence of a higher C_{4v} symmetry between topological phases ruled by C_{2v} class.

V. TIME-DEPENDENT ANALYSIS

A striking feature of the $k_{x/y} \approx \pi$ edge state is its complete localization for any finite value of the hopping amplitudes. This may lead to an enhanced protection of the state when time-dependent perturbations are introduced in the system. Let us consider the square Lieb lattice of Fig. 2(c) and time-dependently vary the dimerization to adiabatically transform this edge eigenstate to a corner eigenstate (moving along the $k_y \approx \pi$ line in Fig. 2). We see from Fig. 8(a) that the projection onto the corner eigenstates, Φ, can be made arbitrarily close to 1 by increasing the time of the adiabatic ramp of the hopping elements. This indicates that this evolution is not affected by the other energy levels and there are no avoided level crossings when this state goes through the bulk band as usual for an adiabatic time-evolution, (with the exception of the transition point). For small lattice sizes the scheme benefits from the finite difference in the energy levels, thus increasing the robustness of the state for each ramp. Nevertheless, this effect saturates when the size of the lattice is increased beyond 15×15 plaquettes. This leads us to suggest that these edge states are greatly protected from mixing with the bulk eigenstates, irrespective of the size of the lattice, by the destructive interference effect that generates a mismatch of the probability density distribution with the bulk eigenstates.

When we apply a fast ramping process [see Fig. 8(b)] some mixing with the other eigenstates occurs. However, the mixing only happens with states that have a large density overlap with the edge states and we can see from Fig. 8 c) that even for fast ramps there is a protection against mixing with a large class of states, resulting in non-avoided energy crossings with the time-dependent target state. This illustrates that these edge states are partially protected against mixing with the bulk states even for large time-dependent perturbations to the hopping amplitudes. However, it should be noted that if we apply a random disorder to either the onsite energies or the hopping terms, then this protection is lost. This leads us to suggest that these states are only protected against perturbations that do not break the destructive interference condition. These time-dependent manipulations of the Hamiltonian can be easily implemented in an experimental realization with cold atoms in an optical lattice [38]. In this experimental context varying the hopping amplitudes throughout the adiabatic ramps is straightforwardly performed by changing the depth of the lattice, which involves controlling the laser power with an acousto-optic modulator (AOM). For appropriate choices of atoms, the interaction strength can also be precisely tuned through Feshbach resonances [39] by varying an applied mag-

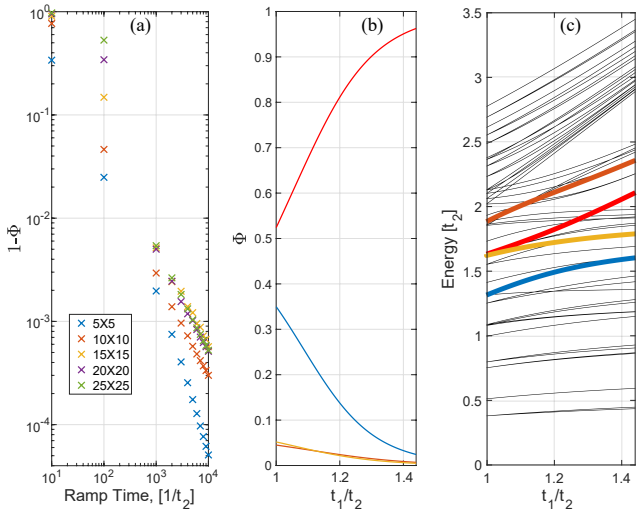

Figure 8. Time-dependent adiabatic transformation of an edge eigenstate into a corner eigenstate for the square rotated Lieb lattice with open boundary conditions. We begin in the positive energy $k_y = \pi$ eigenstate highlighted in red in Fig. 6, and adiabatically ramp the hopping amplitudes from $t_1/t_2 = 2$ to $t_1/t_2 = 1$. (a) Projection of the final produced state onto all corner eigenstates of the final Hamiltonian ($t_1/t_2 = 1$) as a function of the adiabatic ramp time and for a variety of system sizes. (b) Projection of time-dependent state onto the other eigenstates for a fast ramp time ($T = 5t_2$) on a lattice with 5×5 plaquettes. (c) Projections displayed on the energy spectrum, color coded to match (b). All calculations carried out with exact diagonalization and for a time step of $dt = 0.01t_2$.

netic field. The ability to manipulate the potential or remove atoms in order to being with an atom on a specific site enables the preparation of multiple atoms in eigenstates of the system including the initial $k_y \approx \pi$ edge state for $t > 1$, using similar manipulations of the Hamiltonian and beginning with the particle localized on a single site on the edge. Note that this preparation scheme can be applied to more than a single particle (either bosons or fermions) as long as they are non-interacting. Furthermore, we have shown that, in certain conditions, we can time dependently map the $k = \pi$ edge state into a corner eigenstate, offering us a way to also prepare the corner states. With this, we have the tools to experimentally probe and/or verify the stated topological properties of the boundary states for these Lieb-type systems, with or without interactions between particles.

VI. CONCLUSION

In this paper, we have addressed the Lieb lattice with staggered hopping terms and a particular choice of open boundary conditions which reduces its symmetry to C_{2v} class generating weak topological behavior. We demonstrated the existence of unusual boundary states that reflect the interplay of topological protection and geometrical frustration. These states display extreme localization at the vertical or horizontal boundaries (with momentum $k_y \approx \pi$ or $k_x \approx \pi$, respectively) and do not converge into the band gap closing point at the topological transition point, reflecting the existence of a topological non-trivial phase for any value of the hopping parameters. This is in contrast to the usual boundary modes that exhibit a common topological phase transition at the gap closing point with a clear distinction between non-trivial and trivial phases. The former are, in good approximation, the boundary modes $k_y = \pi$ and $k_x = \pi$ of the Lieb ribbons with PBC in the x-direction for $t_1 > t_2$ and in the y-direction for $t_1 < t_2$. The density mismatch of these states and bulk states confers the former protection against time dependent perturbations that change the hopping amplitudes ratio.

For our choice of open boundary conditions, corner states emerge from the latter states due to a higher symmetry class C_{4v} transition point between topological phases ruled by C_{2v} class. This suggests the existence of a quadrupole moment at a single point of the ratio t_1/t_2, but hidden due to immersion of the corner states into the bulk bands.

VII. ACKNOWLEDGMENTS

This work is funded by FEDER funds through the COMPETE 2020 Programme and National Funds through FCT - Portuguese Foundation for Science and Technology under the project UID/CTM/50025/2013 and under the project PTDC/FIS-MAC/29291/2017. AMM acknowledges the financial support from the FCT through the grant SFRH/PD/BD/108663/2015 and through the work contract CDL-CTTRI-147-ARH/2018, and from the Portuguese Institute for Nanostructures, Nanomodelling and Nanofabrication (I3N) through the grant BI/UI96/6376/2018. RGD appreciates the support by the Beijing CSRC. LM acknowledges the financial support from the FCT through the grant BI-32(23331/2018). Work at the University of Strathclyde was supported by the EPSRC Programme Grant DesOEQ (EP/P009565/1).

[1] Wladimir A. Benalcazar, B. Andrei Bernevig, and Taylor L. Hughes. Electric multipole moments, topological multipole moment pumping, and chiral hinge states in crystalline insulators. *Phys. Rev. B*, 96:245115, 2017.

[2] Frank Schindler, Ashley M. Cook, Maia G. Vergniory, Zhijun Wang, Stuart S. P. Parkin, B. Andrei Bernevig, and Titus Neupert. Higher-order topological insulators. *Science Advances*, 4(6), 2018.

[3] Eslam Khalaf. Higher-order topological insulators and superconductors protected by inversion symmetry. 97, 01 2018.

[4] E. Arévalo and L. Morales-Molina. Geometrical frustration in nonlinear photonic lattices. *Phys. Rev. A*, 98:023864, Aug 2018.

[5] Marc D. Schulz and Fiona J. Burnell. Frustrated topological symmetry breaking: Geometrical frustration and anyon condensation. *Phys. Rev. B*, 94:165110, Oct 2016.

[6] R. G. Dias A. M. Marques. Generalization of Zak's phase for lattice models with non-centered inversion symmetry axis. 2017.

[7] Liu Zheng, Liu Feng, and Wu Yong-Shi. Exotic electronic states in the world of flat bands: From theory to material. *Chinese Physics B*, 23(7):077308, 2014.

[8] J. Arkinstall, M. H. Teimourpour, L. Feng, R. El-Ganainy, and H. Schomerus. Topological tight-binding models from nontrivial square roots. *Phys. Rev. B*, 95:165109, Apr 2017.

[9] E. Meyer M. Heinrich O. Zilberberg A. Szameit M. Kremer, I. Petrides. Non-quantized square-root topological insulators: a realization in photonic Aharonov-Bohm cages. 2018.

[10] Bikashkali Midya, Wiktor Walasik, Natalia M. Litchinitser, and Liang Feng. Supercharge optical arrays. *Optics Letters*, 43(20):4927, oct 2018.

[11] Zhifeng Zhang, Mohammad Hosain Teimourpour, Jake Arkinstall, Mingsen Pan, Pei Miao, Henning Schomerus, Ramy El-Ganainy, and Liang Feng. Experimental realization of multiple topological edge states in a 1d photonic lattice. *Laser & Photonics Reviews*, 13(2):1800202, jan 2019.

[12] G. Pelegrí, A. M. Marques, R. G. Dias, A. J. Daley, V. Ahufinger, and J. Mompart. Topological edge states with ultracold atoms carrying orbital angular momentum in a diamond chain. *Physical Review A*, 99(2), feb 2019.

[13] G. Pelegrí, A. M. Marques, R. G. Dias, A. J. Daley, J. Mompart, and V. Ahufinger. Topological edge states and aharanov-bohm caging with ultracold atoms carrying orbital angular momentum. *Physical Review A*, 99(2), feb 2019.

[14] Flore K. Kunst, Guido van Miert, and Emil J. Bergholtz. Lattice models with exactly solvable topological hinge and corner states. *Phys. Rev. B*, 97:241405, Jun 2018.

[15] Flore K. Kunst, Guido van Miert, and Emil J. Bergholtz. Boundaries of boundaries: A systematic approach to lattice models with solvable boundary states of arbitrary codimension. *Phys. Rev. B*, 99:085426, Feb 2019.

[16] Flore K. Kunst, Guido van Miert, and Emil J. Bergholtz. Extended bloch theorem for topological lattice models with open boundaries. *Phys. Rev. B*, 99:085427, Feb 2019.

[17] Michael Springborg, Bernard Kirtman, and Yi Dong. Electronic polarization in quasilinear chains. *Chemical Physics Letters*, 396(4-6):404–409, oct 2004.

[18] Konstantin N. Kudin, Roberto Car, and Raffaele Resta. Berry phase approach to longitudinal dipole moments of infinite chains in electronic-structure methods with local basis sets. *The Journal of Chemical Physics*, 126(23):234101, jun 2007.

[19] Cristiane Morais Smith Guido van Miert, Carmine Ortix. *2D Mater., 4(1):015023*. 2017.

[20] Jun-Won Rhim, Jan Behrends, and Jens H. Bardarson. Bulk-boundary correspondence from the intercellular zak phase. *Physical Review B*, 95(3), jan 2017.

[21] Kuan-Sen Lin and Mei-Yin Chou. Topological properties of gapped graphene nanoribbons with spatial symmetries. *Nano Letters*, 18(11):7254–7260, oct 2018.

[22] Feng Mei, Shi-Liang Zhu, Zhi-Ming Zhang, C. H. Oh, and N. Goldman. SimulatingZ2topological insulators with cold atoms in a one-dimensional optical lattice. *Physical Review A*, 85(1), jan 2012.

[23] Li-Jun Lang, Xiaoming Cai, and Shu Chen. Edge states and topological phases in one-dimensional optical superlattices. *Physical Review Letters*, 108(22), may 2012.

[24] Shi-Liang Zhu, Z.-D. Wang, Y.-H. Chan, and L.-M. Duan. Topological bose-mott insulators in a one-dimensional optical superlattice. *Physical Review Letters*, 110(7), feb 2013.

[25] Xizhou Qin, Feng Mei, Yongguan Ke, Li Zhang, and Chaohong Lee. Topological magnon bound states in periodically modulated heisenberg XXZ chains. *Physical Review B*, 96(19), nov 2017.

[26] V M Martinez Alvarez and M D Coutinho-Filho. Edge states in trimer lattices. 2018.

[27] C. Weeks and M. Franz. Topological insulators on the Lieb and perovskite lattices. *Phys. Rev. B*, 82:085310, 2010.

[28] Wei-Feng Tsai, Chen Fang, Hong Yao, and Jiangping Hu. Interaction-driven topological and nematic phases on the Lieb lattice. *New Journal of Physics*, 17(5):055016, 2015.

[29] Roger S. K. Mong, Jens H. Bardarson, and Joel E. Moore. Quantum transport and two-parameter scaling at the surface of a weak topological insulator. *Phys. Rev. Lett.*, 108:076804, Feb 2012.

[30] Ching-Kai Chiu, Jeffrey C. Y. Teo, Andreas P. Schnyder, and Shinsei Ryu. Classification of topological quantum matter with symmetries. *Rev. Mod. Phys.*, 88:035005, 2016.

[31] Liang Fu and C. L. Kane. Topological insulators with inversion symmetry. *Phys. Rev. B*, 76:045302, 2007.

[32] Michael P. Marder. *Condensed matter physics*. Wiley, 2010.

[33] A. A. Lopes and R. G. Dias. Interacting spinless fermions in a diamond chain. *Phys. Rev. B*, 84:085124, 2011.

[34] Bikashkali Midya, Wiktor Walasik, Natalia M. Litchinitser, and Liang Feng. Supercharge optical arrays. *Opt. Lett.*, 43(20):4927–4930, Oct 2018.

[35] Sonja Barkhofen, Lennart Lorz, Thomas Nitsche, Christine Silberhorn, and Henning Schomerus. Supersymmetric polarization anomaly in photonic discrete-time quantum walks. *Phys. Rev. Lett.*, 121:260501, Dec 2018.

[36] S. J. Barnett. On the Theory of Diamagnetism. *Phys. Rev.*, 25:835–840, 1925.

[37] Kohei Kawabata, Ryohei Kobayashi, Ning Wu, and Hosho Katsura. Exact zero modes in twisted kitaev chains. *Phys. Rev. B*, 95:195140, May 2017.

[38] Immanuel Bloch, Jean Dalibard, and Wilhelm Zwerger. Many-body physics with ultracold gases. *Rev. Mod. Phys.*, 80:885–964, Jul 2008.

[39] Cheng Chin, Rudolf Grimm, Paul Julienne, and Eite Tiesinga. Feshbach resonances in ultracold gases. *Rev. Mod. Phys.*, 82:1225–1286, Apr 2010.